Tutorial

Phase-Boundary Mapping to Engineer Defects in Thermoelectric Materials

Leah Borgsmiller, Duncan Zavanelli, and G. Jeffrey Snyder*
Northwestern University, Department of Materials Science and Engineering, Evanston, IL 60208, USA

(Received 7 June 2022; revised 12 August 2022; published 15 September 2022)

The optimization of thermoelectric materials for use in various applications, such as spacecraft power generation, waste heat recovery, and Peltier coolers, requires a careful optimization of material properties. This can be achieved via defect engineering in which defects are purposefully added to a material to produce desired properties. In this tutorial, we discuss a defect engineering strategy called phase-boundary mapping. While many compound thermoelectric semiconductors are often called "line compounds" due to their appearance as a line on a binary phase diagram, in reality, due to the laws of thermodynamics, all phases have a finite phase width. The edges of this phase space define the chemical potential of the material. By making small compositional changes across this phase space, appreciable differences in thermoelectric properties are observed due to this change in the chemical potential. Additionally, the phase equilibria of a thermoelectric material impacts alloying and dopability that further impacts material properties. Phase-boundary mapping is a strategy that allows us to explore the limits of a material and ultimately reproducibly optimize thermoelectric performance by considering the effects of off-stoichiometry on chemical potential, and thus defect energies and material properties. This technique can be applied in the optimization of numerous thermoelectric materials as well as extended to other semiconductors with properties controlled by defects.

DOI: 10.1103/PRXEnergy.1.022001

I. INTRODUCTION

Thermoelectrics are solid-state semiconductor devices that convert a temperature gradient to electricity and vice versa [1]. In the power generation mode, thermoelectrics convert heat to electricity, allowing for electricity generation for applications such as spacecrafts and remote power sources where other power generation technologies are not possible. Thermoelectrics have historically been used in the radioisotope thermoelectric generators that power the deep space probes such as Voyager and more recently on the Mars rovers [2]. In the future, thermoelectrics could be used to convert waste heat to electricity [3,4] in a variety of processes, such as in energy intensive industrial processes or in the engine of a vehicle [5]. Thermoelectrics can also be used in reverse where applied electricity can generate a temperature gradient. Under these operating conditions, thermoelectric devices can replace harmful refrigerants with a safer solid-state alternative such as a Peltier cooler [6]. Compact thermoelectric devices can efficiently supply small temperature difference heating and cooling immediately to where it is needed, such as seat heating and cooling [4]. Such zonal heating, ventilation, and air conditioning [7] designs could lead to system efficiency improvements over traditional designs. The benefit of thermoelectrics compared with other forms of renewable energy is that there are no moving parts, no necessary maintenance, they have a long device life, and they have good scalability [8].

Thermoelectric materials, along with many other semiconductor materials, are often considered to be line compounds in that they appear as a line on a phase diagram. However, due to the laws of thermodynamics, all line compounds on a phase diagram actually have a finite width [9]. In the practical synthesis of materials, oftentimes materials are not synthesized perfectly in this single-phase region and thus a sample is usually bound to be in thermodynamic equilibrium with impurity phases defined by the phase space [10]. In fact, such phase or solubility boundaries can be conveniently used to achieve optimal dopant concentrations such as in $(Bi,Sb)_2Te_3$ [11] and Yb_xCoSb_3 [12]. Ultimately, all thermoelectric materials can be synthesized into at least two different thermodynamic states that are set by the chemical potentials of the different phases in equilibrium on the phase diagram. These possible thermodynamic states lead to different defect concentrations [13] and dopant solubilities [14] that in turn impact overall thermoelectric performance.

Here we discuss a systematic approach called phase-boundary mapping in which the different thermodynamic states of a single thermoelectric material are explored [15]. By purposefully introducing secondary phases or by

*jeff.snyder@northwestern.edu

otherwise setting the chemical potential of a thermoelectric material, the equilibrium phase region can be set, allowing us to identify the phase-region-dependent properties and thus allow for reproducible optimization of a given thermoelectric material. Methods for setting the chemical potential to achieve reproducible optimization will be discussed in greater detail throughout this tutorial. In recent years, phase-boundary mapping has shown to be an incredibly useful tool in improving and understanding thermoelectric performance in a variety of different material systems [16–19]. Additionally, the phase-boundary mapping approach is not limited to the study of thermoelectric materials, and could be used to engineer defects in a variety of other valence precise compounds, including semiconducting and intermetallic materials for various applications.

In this tutorial, we first discuss relevant metrics and quantities to understand thermoelectric performance. Then we consider doping and how dopants can impact material properties and overall thermoelectric performance. We then introduce the concept of phase-boundary mapping from a thermodynamic standpoint, utilizing schematic phase diagrams. Real examples of phase-boundary mapping in a variety of both binary and more complicated multinary systems follow. Finally, this tutorial closes with a section outlining practical steps and considerations that can be used as a guideline for future phase-boundary mapping studies.

II. THE IDEAL THERMOELECTRIC MATERIAL

The efficiency of a thermoelectric material is often measured using the dimensionless figure of merit, called zT [1]. For practical thermoelectric materials, zT has historically been around 1; however, advances in the field in the last few decades has led to higher zT values [20–22]. The zT material figure of merit is calculated using the Seebeck coefficient α, the electrical conductivity σ, and the thermal conductivity κ [1]:

$$zT = \frac{\alpha^2 \sigma T}{\kappa}. \tag{1}$$

The Seebeck coefficient α is a measure of the voltage generated by a temperature difference resulting from the Seebeck effect. For small ΔT, the Seebeck coefficient can be written as

$$\alpha = \frac{\Delta V}{\Delta T}. \tag{2}$$

The Seebeck coefficient is related to the number density of charge carriers in the material, n [23]. For metals or degenerate semiconductors, $\alpha \sim n^{-2/3}$ [24]. In order to have an efficient thermoelectric material with a large Seebeck coefficient, there should be only one dominant charge carrier type because bipolar conduction reduces the Seebeck coefficient [1]. Thus, as the number of charge carriers increases, the Seebeck coefficient decreases. However the opposite is true for the electrical conductivity σ, where the electrical conductivity increases with an increasing number of charge carriers ($\sigma \sim n$).

From these relationships between carrier concentration and the Seebeck coefficient and electrical conductivity, we can see that there is a conflicting requirement for the charge carrier concentration n. Similarly, while it is desirable to have a high electrical conductivity, as often seen in crystalline materials, the thermal conductivity should be low. This leads to the general description of an ideal thermoelectric as an "electron crystal-phonon glass" [25].

The total thermal conductivity of a material is given by contributions from the lattice thermal conductivity and the electrical thermal conductivity. The electrical contribution to the thermal conductivity is directly related to the electrical conductivity σ via the Wiedemann-Franz approximation using the Lorenz number L. Thus, the electronic contribution to the thermal conductivity is also a function of charge carrier concentration n. The lattice thermal conductivity can be suppressed however in order to increase zT using various phonon engineering techniques, such as introducing scattering centers [26–30]:

$$\kappa \approx \kappa_l + \kappa_e = \kappa_l + L\sigma T. \tag{3}$$

By considering the effects of the charge carrier concentration on the various components for zT (α, σ, and κ), we can see the zT of a material peak at an optimal charge carrier concentration (Fig. 1).

Since reaching the maximum value of zT requires an optimal carrier concentration, comparing the zT for unoptimized materials is not an ideal point of comparison. Independent of n, a complementary strategy is to increase the quality factor B, which also depends on defects. The quality factor B is proportional to the weighted mobility μ_w and inversely proportional to the lattice thermal conductivity κ_l [32–34]:

$$B \sim \frac{\mu_w}{\kappa_l}. \tag{4}$$

The weighted mobility can be calculated as a function of the Seebeck coefficient and the electrical conductivity and is inspired by the parabolic band model [35]. Thus, B can be calculated for a given material at a specific temperature using only measured values of the Seebeck coefficient, the electrical conductivity, and the lattice thermal conductivity [34]. While optimizing the zT of a material is often the goal in thermoelectric material improvement, considering the material quality factor B is a good way to gauge a material's potential to reach high zT values. The higher the value of B, the higher the maximum value of zT a material

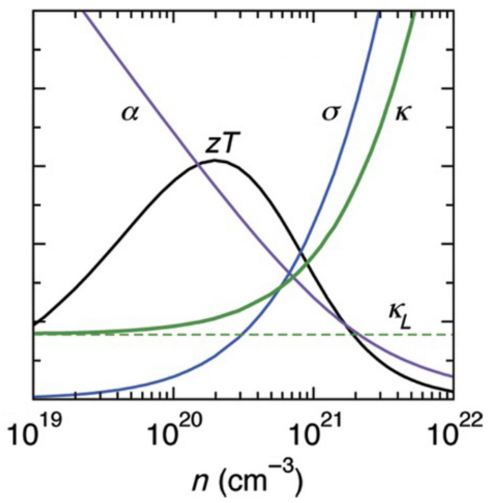

FIG. 1. Plots of α, σ, and κ versus the carrier concentration n, as well as the resulting zT. Since all of the components of zT depend on the carrier concentration, the zT of a material will peak at a single value of the carrier concentration. Adapted with permission from E. S. Toberer *et al.*, Chem. Mater. 22, 624 (2010). Copyright 2009. American Chemical Society.

can obtain given optimal doping. Since this quality factor is dependent on the lattice thermal conductivity, efforts to decrease κ_l such as through alloy scattering can increase B as long as μ_w is not reduced to a greater extent than κ_l. The improvement of thermoelectric materials is thus a complicated multidimensional optimization problem that must consider numerous factors and material properties. The optimization of quantities such as n and B simplifies this complexity because by increasing B and doping to an optimal n, maximum zT for a material can be achieved. Of course, this approach is still not trivial. While defects are capable of drastically changing n, they may also impact the thermoelectric quality factor B and such competing effects are still essential to consider. Phase-boundary mapping is a strategy that we show can drastically impact the defects in a material, which can impact both B and n, and thus can be used as a tool to optimize thermoelectric performance.

III. CHARGE CARRIER TUNING THROUGH DOPANTS AND DEFECTS

In any thermoelectric device, there are both n-type and p-type semiconductor legs, with the n-type legs having excess electrons and the p-type legs having excess holes at the optimal charge carrier concentrations.

Achieving the optimal carrier concentration generally requires the doping of a material through addition of other elements or the convenient use of solubility and phase boundaries [11,37] to increase or decrease the number of holes or electrons. The effect of doping is often understood through simple valence balance. For instance, replacing Te (valency of −2) with I (valency of −1) in PbTe increases the number of free electron charge carriers in the system, Thus, I can be used as an n-type dopant in PbTe [14].

While doping is a great way to adjust the charge carrier concentration, the selection of dopant materials is not always straightforward. The selection of a dopant type can have noticeable effects on device performance and ultimately zT. It has been shown that in order to have the smallest effect on the charge carrier mobility, it is best to use a cation acceptor for p-type materials and an anion donor for n-type materials [38].

The choice of dopant atoms is also impacted by the types of intrinsic defects that are energetically favorable in the system. Figure 2 shows some possible intrinsic defects in a sample compound MX as well as a description of the defect using Kröger-Vink notation [36]. Kröger-Vink notation is a way of symbolically representing defects. Subscripts indicate the site of a particular atom or vacancy (denoted by V), and the superscripts indicate the charge on that species, with dots indicating positive charge and apostrophes indicating negative charge. The defects shown here include cation vacancies, anion vacancies, cation interstitials, anion antisites, and cation antisites [39,40]. Generally, these point defects are charged and thus impact the charge carrier concentration. For instance, in the case of a cation vacancy as shown in Fig. 2(a), the missing cation from the crystalline lattice results in the addition of a free charge carrier in the form of a hole to charge balance the system, as shown in this figure using Kröger-Vink notation [36]. This cation vacancy can make the material more p type, whereas anion vacancies as shown in Fig. 2(b) lead to excess electrons resulting from the missing X^{-1} ion. Figure 2(c) depicts a cation interstitial. Anion interstitials are not included in this schematic because they are often unlikely due to geometric constraints from the larger anion radius. Figures 2(d) and 2(e) show antisite defects in which an atom is on the site that is regularly occupied by the other atom. These antisite defects are both intrinsic, in that the atoms are both native to the compound. Extrinsic interstitial and antisite defects occur when additional elements are added to the system as dopants or perhaps accidentally as contaminates.

Depending on the type of defect, a material may either gain excess electrons or excess holes, thus pushing the Fermi level E_F towards the conduction band or valence band, making the sample n type or p type, respectively. Because these defects are adding additional holes and/or electrons, they are impacting the material's charge carrier concentration n. These defects thus dictate the material's thermoelectric properties, as shown in Fig. 1. For instance, if a material had anion vacancies as the dominant defect, there would be additional free electron charge carriers. If the number of anion vacancies increased, the charge carrier concentration n would also increase, resulting in an increase in electrical conductivity and total thermal

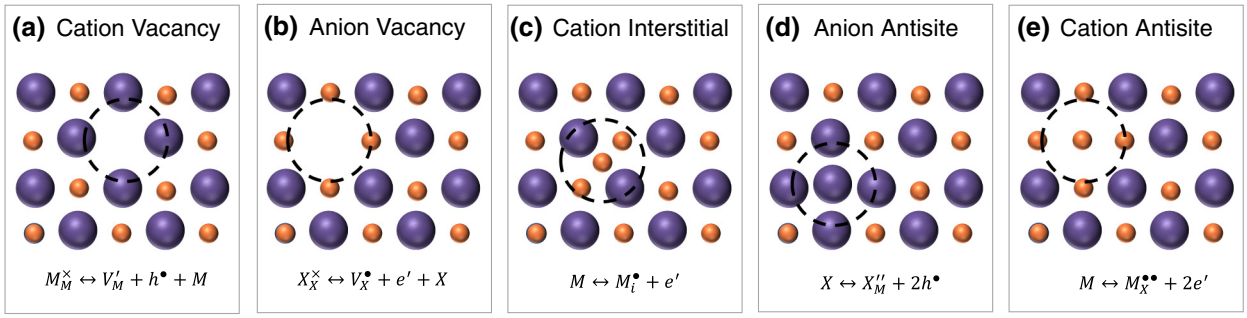

FIG. 2. Some possible intrinsic point defects in a sample MX crystal. In this general case, the ionic charges are considered to be $+1$ and -1, respectively. Within each panel there is a schematic of the crystal structure with the defect circled and the Kröger-Vink notation [36] balanced defect reaction that shows whether the defect leads to additional free holes or electrons. The intrinsic defects shown here are a cation vacancy (a), an anion vacancy (b), a cation interstitial (c), an anion antisite defect (d), and a cation antisite defect (e).

conductivity, but also a decrease in the Seebeck coefficient. Thus, control over the dopants offers control over thermoelectric properties.

An extrinsic dopant's ability to dope a system (its dopability) can depend heavily on the intrinsic defects found naturally in the material. Different defects, both intrinsic and extrinsic, have differing defect formation energies that dictate the dominant defect in a material [13]. As we show later, these defect energies can differ for the same nominal compound, depending on the thermodynamic state of the material. Additionally, point defects can affect other aspects of the system, including diffusion and kinetics [41–43], mechanical properties [44–46], electronic transport [47,48], and thermal transport [49,50].

IV. PHASE DIAGRAMS AND A THERMODYNAMIC DESCRIPTION OF PHASE-BOUNDARY MAPPING

Phase-boundary mapping is an approach in which different thermodynamic states of the same nominal compound are systematically studied. These different thermodynamic states arise from the differing chemical potential values set by phase equilibria within different regions of a phase diagram. These differing chemical potentials then set the defect formation energies that in turn impact numerous properties, often through changing the charge carrier concentration. Additionally, these differing chemical potentials can impact other properties of the system. For instance, the thermal conductivity and band structure of a material can be impacted by defects even if these defects are uncharged [55].

Phase-boundary mapping was first used as a term by Ohno *et al.* [51] for the optimizations of $Ca_9Zn_{4+x}Sb_9$ [15] and Mg_3Sb_2; however, the underlying concepts have been observed and utilized previously for other types of material systems without using this term specifically [12,54,56–59]. It has since been used for dozens of thermoelectric material studies. This methodology can be understood schematically by looking at Fig. 3. In this case we are considering an arbitrary binary compound, A_xB_y, where A and B are the constituent atoms and the stoichiometry is set by x and y. In Fig. 3(a), there is a sample binary eutectic phase diagram. The compound of interest A_xB_y appears to be a line compound with an infinitesimal width. However, in Fig. 3(b) we see that there is a finite width of the compound, although it is too narrow to see on the full phase diagram in Fig. 3(a). This finite width is a result of intrinsic defects within the material. These intrinsic defects are unavoidable in any material at finite temperature due to the laws of thermodynamics [60]. The free energy of a system is given by the relation

$$G = H - TS, \tag{5}$$

where G is the free energy, H is the enthalpy, T is the temperature, and S is the entropy. The entropy of a system increases as the number of defects increases and thus there is some defect concentration that minimizes the free energy dependent on the enthalpy of the compound [9]. These inevitable defects necessitate a finite phase width. Since the finite width of the compound is very small, samples made in the lab will practically be either A excess or B excess. In this tutorial we use the term "excess" to indicate there being more of a particular element than in the nominal composition. It does not mean that the compound is majority that element. Some phase-boundary mapping studies use the terms "rich" or "poor" to describe these states. In this example where there are no additional phases between the A_xB_y compound and elemental phases A and B, if a sample is A excess, its chemical potential will be set by pure A and the compound A_xB_y. If a sample is B excess, its chemical potential will be set by pure B and the compound A_xB_y. Thus, for the nominal binary compound A_xB_y, there are two distinct thermodynamic states, A excess and B excess.

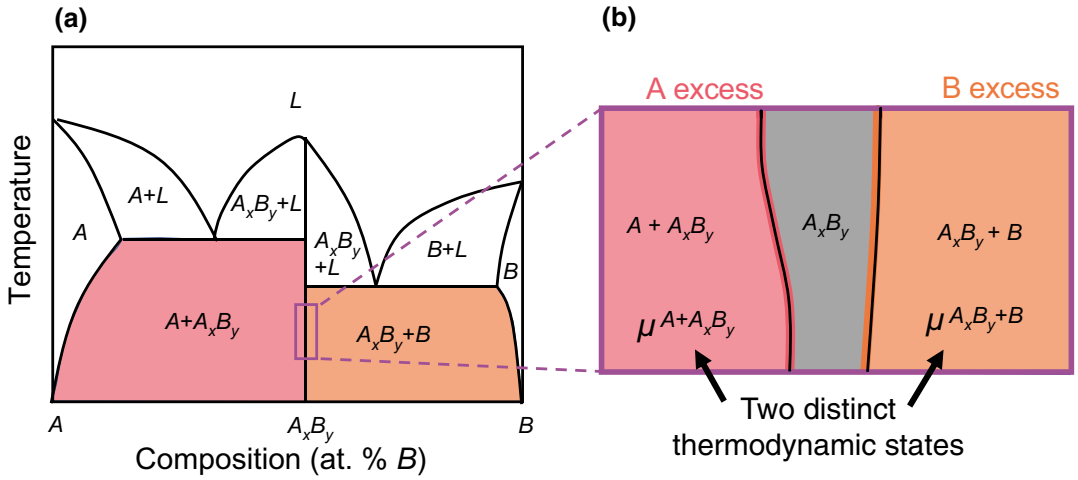

FIG. 3. Schematic demonstrating the importance of phase-boundary mapping in a sample binary system [10,51] with an arbitrary binary compound of interest, A_xB_y, where A and B are the constituent atoms and the stoichiometry is set by x and y. (a) A sample binary eutectic phase diagram where A_xB_y appears to be a line compound. (b) An enlarged view of a region of the phase diagram showing that A_xB_y actually has a finite width. The two phase regions, A excess and B excess, have different chemical potentials μ.

This approach is informed by the Gibbs phase rule that is often written as

$$F = C - P, \tag{6}$$

where F is the degrees of freedom, C is the number of components, and P is the number of phases [61]. This formulation of the Gibbs phase rule is at constant temperature and pressure.

In this binary case, there are two components, A and B. Thus, samples made in one of the two-phase regions shown in the phase diagram in Fig. 3(a) (colored in pink and orange) will have zero degrees of freedom. This means that a sample synthesized in a two-phase region in a two component system will have fixed composition set by the two phases in that region. For instance, a sample made slightly A excess will be primarily A_xB_y phase with some secondary A phase with the mole fractions of these two phases dictated by the binary lever rule [62]. The binary lever rule uses the ratios of the distances in phase space between a given composition and the equilibrium phases to determine the fraction of constituent phases for that composition. There is an analogous formulation of the lever rule for ternary systems as well.

The effect of the chemical potential on defects present in a sample can be considered using the law of mass action and energetics of defect formation. For instance, consider the hypothetical phase A_xB_y shown in Fig. 3. Let us consider the case where A vacancies are the most prevalent intrinsic defect. Let us also assume that the A vacancy has a charge of -1, such as shown in Fig. 2(a). The chemical equation describing this situation is

$$A_xB_y \rightarrow A_{x-\delta}B_y + \delta A(s) + \delta h^+. \tag{7}$$

The defect formation energy for a single A vacancy (V_A) can then be determined by calculating the difference in energy between the products and the reactants. This includes the energy difference between the defective and pristine structure, as well as the energy contributions of the two products, the hole and the removed A atom [13,63]. The energy of the hole is the negative of the chemical potential of the electron (the Fermi level E_F), and the energy of the removed A atom is the same as the chemical potential of A. The difference in the energies between the pristine structure and the defective structure can be calculated using density functional theory (DFT) calculations. Thus, the defect formation energy for an A vacancy can be written as [56,64,65]

$$\Delta E_{V_A} = E_{\text{defective}} - E_{\text{pristine}} - E_F + \mu_A. \tag{8}$$

While this expression is specific to the case of an A vacancy with a -1 charge, similar expressions can be written for all types of defects. The important takeaway is that defect energies depend on values such as the Fermi level and the chemical potential of the relevant species.

The concentration of any defect in a material is directly related to the defect energy of formation for that defect by the relation

$$x_{\text{defect}} = x_0 \exp\left(-\frac{\Delta H_{\text{defect}}}{kT}\right), \tag{9}$$

where x_0 is the concentration of possible defect sites [40]. Thus, the concentration of a specific type of defect in a material is highly dependent on the defect formation energy that is directly impacted by the chemical potential. Since the chemical potential varies depending on the

phase region of synthesis, whether a sample is A excess or B excess can have great impacts on the defect concentration. It should be noted that here we are highlighting the simplest case with dilute noninteracting defects. In a real material there may be many different competing defects with differing relationships between the defect formation energy and the equilibrium Fermi level. The overall equilibrium Fermi level and the concentration of charge carriers in the material can be determined by considering all of the different defects present in the material and their respective contributions and interactions.

Charge transport in thermoelectric semiconductors is determined by the free charge carrier concentration that is set by defects and dopants within the material. In this example, the A-excess and B-excess A_xB_y samples will have different defect concentrations and possibly different charge carrier concentrations due to the difference in defect formation energies resulting from the differing chemical potentials. In Fig. 1, we show the profound impact that charge carrier concentration has on the thermoelectric properties and ultimately the material zT. Defect concentration can also impact other thermoelectric properties in the material besides carrier concentration, such as the lattice thermal conductivity through point defect scattering [66,67].

Phase-boundary mapping can also be applied to ternary or larger multinary systems, beyond what we have shown thus far with the binary case. Figure 4(a) shows a very simple extension to a ternary phase diagram. In a ternary phase diagram, each triangular region is a three-phase region with zero degrees of freedom by the Gibbs phase rule. Similar to the binary case shown in Fig. 3, the phase region of the compound of interest is quite small and, thus, there are multiple possible thermodynamic states for the same nominal compound as a result of being in chemical equilibrium with different phases. In this simple schematic where the only stable phase in the ternary system is the compound of interest, there are three main thermodynamic states; however, in more complicated ternary spaces, such as the sample phase diagram in Fig. 5, with many phases, there may be many more thermodynamic regions to consider through phase-boundary mapping.

Figure 5 depicts the same arbitrary phase diagram of interest $A_xB_yC_z$, but there are four additional phases in the A-B-C system, marked by squares and denoted α, β, γ, and δ. In this arbitrary phase diagram, α is a binary phase formed with B and C, γ is a binary phase formed with A and B, and β and δ are both ternary phases in the A-B-C system. In the simplest ternary phase diagram case shown in Fig. 4(a), there are only three distinct thermodynamic states to explore using phase-boundary mapping; however, in the more complicated ternary phase diagram with additional stable phases shown in Fig. 5, there are now seven distinct, readily accessible thermodynamic states to consider (there are 15 thermodynamic states if you consider the binary regions and the small single-phase region; however, the phase widths of these regions tend to be incredibly narrow and difficult to reproducibly synthesize). Each of these distinct thermodynamic states may have differing defect concentrations, and thus different thermal and electronic material properties. This demonstrates the complexity of phase-boundary mapping in real systems, and also the importance of using this technique to understand complicated thermoelectric material systems. With

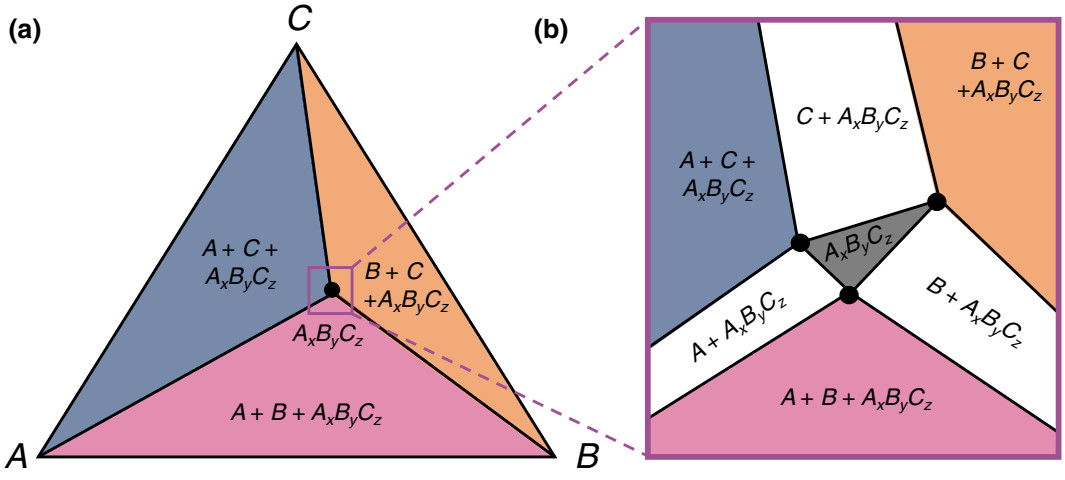

FIG. 4. A simple schematic of phase-boundary mapping for a ternary system as considered in many recent works [10,15–17,52–54]. (a) A sample ternary phase diagram with only one compound, the arbitrary compound of interest $A_xB_yC_z$, with A, B, and C being the constituent atoms and the stoichiometry being set by x, y, and z. In a ternary phase diagram, the triangles are regions of constant chemical potential. (b) An enlarged view of the phase diagram in (a) to show the finite size of the phase region. The three black dots indicate the composition-invariant points (sometimes shortened to c-invariant points [19] or just referred to as invariant points).

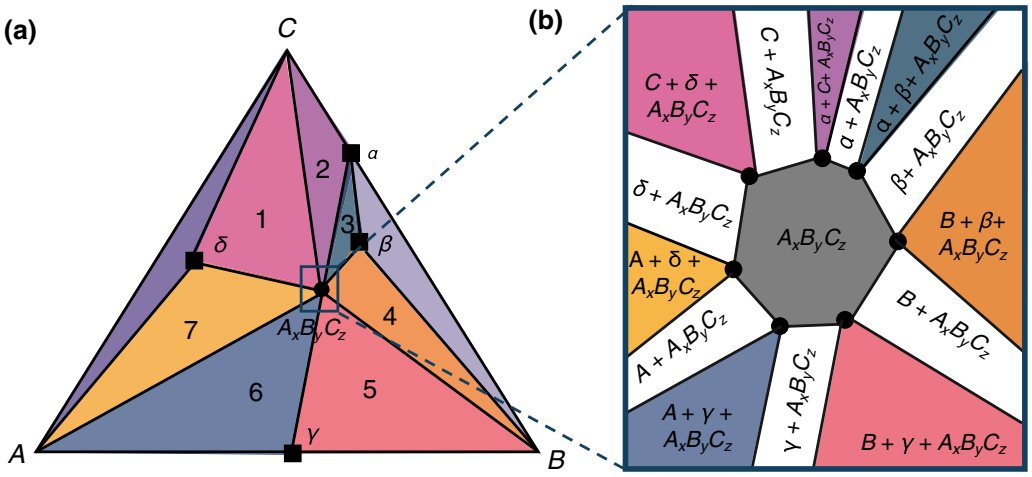

FIG. 5. (a) A more complicated ternary phase diagram consisting of the same compound of interest $A_xB_yC_z$ as shown in Fig. 4, but also four additional phases: α, β, γ, and δ. Increasing the number of stable phases in the system increases the number of distinct thermodynamic states to be considered through phase-boundary mapping. (b) Enlarged view of the phase diagram in Fig. 4(a). The gray region in the middle is the single-phase region, the white regions are the finite-width two-phase regions, and the colored regions are the three-phase regions. Note that to go from any three-phase region to a neighboring three-phase region you must pass through a two-phase region.

large numbers of possible thermodynamic varieties for a single nominal compound, knowledge of the phase equilibria is required for optimized and reproducible material synthesis.

V. PHASE-BOUNDARY MAPPING IN BINARY SYSTEMS

A. Phase-boundary mapping to obtain both *n*-type and *p*-type versions of the same material

PbTe is perhaps the most well-studied thermoelectric material, having been used as early as the 1960s in powering space missions [68–70]. Like most binary thermoelectric semiconductors, it is often considered to be a line compound; however, experimental variations of free charge carrier concentration [71–75] combined with an interpretation of the dominant charged defect [76–78] has been used to determine the finite and asymmetric phase widths of PbTe to be as wide as about an 8×10^{-5} mole fraction.

However, due to the very small magnitude of the phase width, it is nearly impossible to produce phase pure PbTe. Thus, every PbTe sample is either Pb excess or Te excess, and the chemical potential is different for these two "flavors" of PbTe. Male *et al.* [14] demonstrated that Te-excess PbTe samples had a low dopability due to the energetically favorable Pb vacancies in that phase region. They showed that by synthesizing Pb-excess PbTe, they were able to dope *n*-type samples, which is not possible under Te-excess conditions. By switching between synthesizing under Te-rich conditions to synthesizing under Pb-rich conditions, they moved from one phase region to another, similar to switching between the two distinct phase regions in Fig. 3. Synthesizing PbTe under Pb-excess and Te-excess conditions is done using saturation annealing, a technique discussed later in this tutorial. In this case, the effectiveness of dopants at changing the charge carrier concentration is drastically different depending on which phase region the sample is synthesized in. This demonstrates that in order to effectively dope some thermoelectric compounds, knowledge of the phase equilibria and defect energies should be utilized. Other phase-boundary mapping studies of PbTe have been conducted following this initial work [79].

Another key issue in the synthesis of thermoelectric materials is the issue of reproducibility. By deliberately setting the chemical potential as is done in phase-boundary mapping, greater control is given in creating samples with specific properties. Considering once again the example of phase-boundary mapping PbTe, if an experimentalist were to simply combine Pb and Te in the stoichiometric ratio, there would be no real control over whether the sample was equilibrated Pb excess or Te excess, resulting in samples with either favorable or nonfavorable properties randomly. However, in purposefully setting the chemical potential and defect energies via saturation annealing, samples can be consistently synthesized *p* type or *n* type. The semiconductor type in PbTe can even be switched from *p* type to *n* type and vice versa via subsequent saturation annealing steps [14]

Similar to PbTe, consider another well-studied binary thermoelectric, Bi_2Te_3. While the prominent intrinsic

defects in PbTe tend to be vacancies, Bi_2Te_3 tends to be dominated by antisite defects [80–82]. Thus, while Pb-excess PbTe is *n* type due to the suppression of Pb vacancies, Bi-excess Bi_2Te_3 is *p* type due to the Bi atoms on the Te sites antisite defects [11]. In both PbTe and Bi_2Te_3 we see that, depending on which phase region a sample is in, the carrier concentration can be impacted so drastically that it can be made either *p* type or *n* type with very small compositional changes. In Fig. 6 we show that in going from a mole fraction of Te of about 0.5997 to 0.6002, there can be a massive change in the Seebeck coefficient, going from about 235 $\mu V K^{-1}$ (*p* type) to -254 $\mu V K^{-1}$ (*n* type). Here, by crossing a phase boundary, samples can be made with very different properties even with nominal compositions that are incredibly close.

Another example is Mg_3Sb_2. For years, it was believed that only *p*-type Mg_3Sb_2 existed despite various dopant studies [83–85]. However, it has been shown recently that it can be made *n* type when considering this phase-boundary mapping approach [51]. In this material, the dominant intrinsic defect is cation vacancies (Mg vacancies). This defect in many cases can be considered to be a "killer defect." Killer defects have formation energies less than zero, and thus should spontaneously arise in the material [86]. In the case of Mg_3Sb_2, the defect formation energy for Mg vacancies dips below zero towards the conduction band minimum. This defect can essentially pin the Fermi level such that the sample is bound to be *p* type due to the excess holes resulting from the unavoidable Mg-vacancy electron-killer defects. Despite efforts to dope the material *n* type using *n*-type dopants, the resulting samples are persistently *p* type.

Ohno *et al.* [51] demonstrated that by making Mg-excess Mg_3Sb_2, they could reproducibly make *n*-type Mg_3Sb_2 by suppressing the Mg vacancies with the chemical potential in that region set by elemental Mg and Mg_3Sb_2. They showed that because the chemical potential of the system acts like a step function at the line compound boundary, they were also able to observe a step function in the Seebeck coefficient at that point, with the Seebeck coefficient going from positive (*p* type) to negative (*n* type) as the system goes from Sb excess to Mg excess. This step function in the Seebeck coefficient is shown in Fig. 7. Note that here they also included a small amount of Te doping, as is often done to increase the thermoelectric performance in Mg_3Sb_2. In this Mg_3Sb_2 system, as well as in other systems studied by phase-boundary mapping, there is a steplike function of material properties across the phase boundary. This is a result of the step change in chemical potential at the boundary. Once again as was seen for the cases of PbTe and Bi_2Te_3, it is shown here that in binary thermoelectrics the difference between an *n*-type and *p*-type material can sometimes be simply attributed to the sample being cation rich or anion rich and thus fixing the chemical potential and defect formation ability.

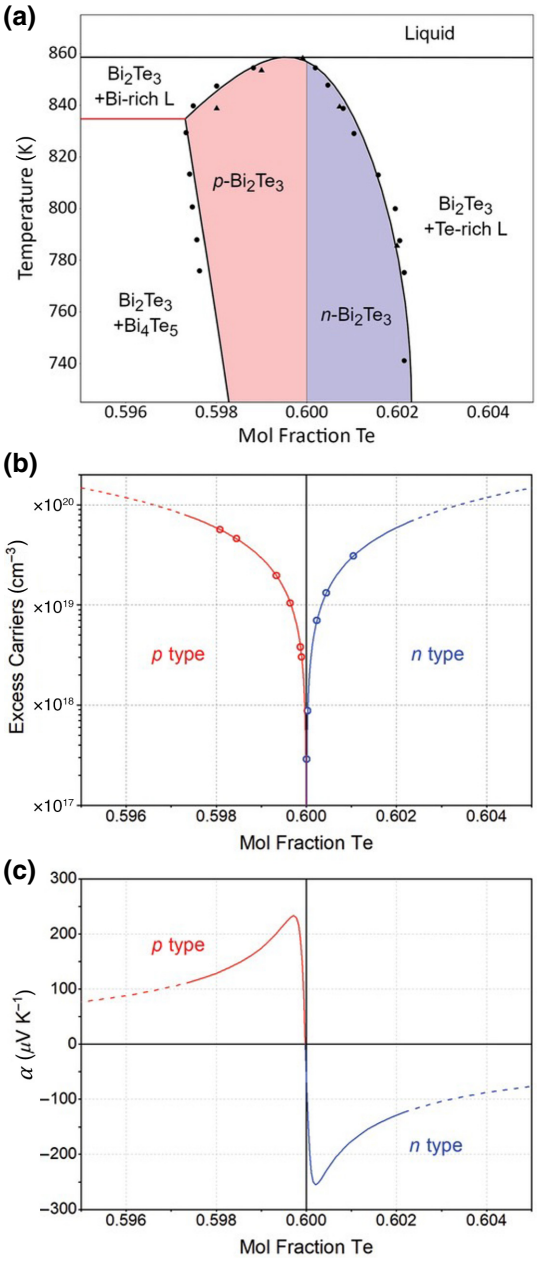

FIG. 6. Phase-boundary mapping considerations of binary Bi_2Te_3. (a) Enlarged binary phase diagram with the small finite width of the single-phase region. (b) Plot of excess charge carriers versus the mole fraction of Te. Te-excess samples are *n* type, whereas Bi-excess samples are *p* type. (c) Seebeck coefficient versus the mole fraction of Te for this same narrow region in the phase diagram about Bi_2Te_3. Small differences in composition make appreciable differences in the value of the Seebeck coefficient. Reprinted and adapted with permission from I. T. Witting *et al.*, Adv. Electron. Mater. 5, 1800904 (2019). Copyright 2019, John Wiley and Sons.

B. Other insights from phase-boundary mapping binary compounds

Not all thermoelectric materials however can be made both *p* type and *n* type using phase-boundary mapping such

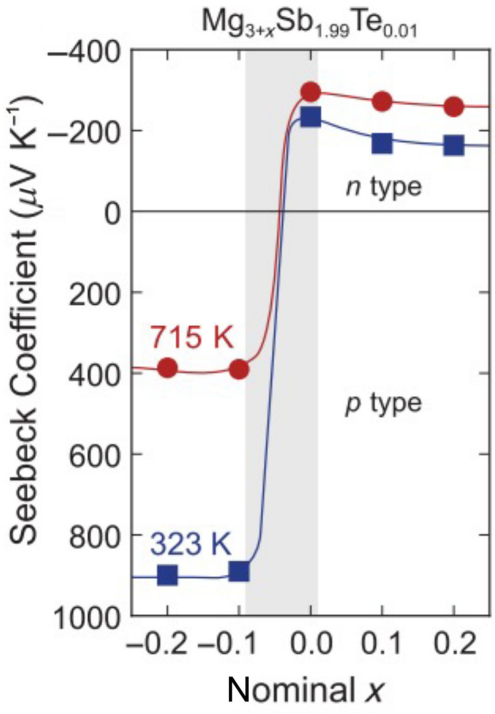

FIG. 7. Step function in the Seebeck coefficient in $Mg_{3+x}Sb_{1.99}Te_{0.01}$ across a small range of x as a result of crossing a phase boundary from Sb excess (p type) to Mn excess (n type) [51]. Similar steplike functions have been shown in other phase-boundary mapping studies such as the step function in the carrier concentration demonstrated in $Ca_9Zn_{4+x}Sb_9$ [15] [Fig. 8(c)] and in $YbZn_2Sb_2$ [87], and the step function in the lattice constant demonstrated in the study of $Yb_xCo_4Sb_{12}$ [59] [Fig. 10(b)]. Reprinted with permission from S. Ohno *et al.*, Joule 2, 141 (2018). Copyright 2018, Elsevier.

as is seen in PbTe, Bi_2Te_3, and Mg_3Sb_2. For some binary systems, only one type of dominant charge carrier is possible, even with changing dopants and chemical potentials. For instance, SnTe and Sb_2Te_3 are always p-type semiconductors. Yet, phase-boundary mapping is still quite useful in the optimization of these materials.

SnTe has been demonstrated to always be a p-type semiconductor [88,89]. This is due to the fact that the single-phase region is offset from the 50 at. % line because of low-energy Sn vacancies that are energetically favorable at any practical temperature. This leads to excess holes regardless of whether the sample is made Sn excess or Te excess. However, although making the sample cation excess or anion excess does not impact the type of semiconductor, there is still a large effect on the charge carrier concentration. If the sample is made Sn rich, there is a relatively low hole concentration, and if the sample is made Te rich, there is a high hole concentration, with a difference of about one order of magnitude between the two [90].

Very similar to SnTe, Sb_2Te_3 is also persistently p type with a hole concentration that depends on whether the system is cation rich or anion rich. This persistent p-type behavior is due to Sb on Te antisite defects that cause the phase stability to always be towards the Sb-rich side of the phase diagram [11]. The concentration of holes in the material depends on whether the material is synthesized Sb rich or Te rich. In these binary examples, it is shown that, through phase-boundary mapping, the charge carrier concentration can be greatly impacted.

VI. PHASE-BOUNDARY MAPPING IN MULTINARY SYSTEMS

Thus far, we have discussed the thermodynamic understanding of phase-boundary mapping and shown how various studies have utilized this technique to better understand binary thermoelectric compounds. Now, we show how this method has been used in ternary and even greater multinary phase spaces. As shown in Fig. 4, the basic understanding of phase-boundary mapping through phase diagrams is not very different from the binary case shown schematically in Fig. 3. However, there is a greater number of distinct thermodynamic states about the compound of interest, particularly in a phase space with multiple stable phases, as shown in Fig. 5. One key ternary study utilizing the phase-boundary mapping approach studied the Zintl thermoelectric compound $Ca_9Zn_{4+x}Sb_9$ [15]. In this work, which is highlighted in Fig. 8, Ohno *et al.* [15] synthesized samples of $Ca_9Zn_{4+x}Sb_9$ with various x values ranging from 0.2 to 0.8. In doing so, they created samples in multiple distinct phase regions and thus thermodynamic states, as shown in Figs. 8(a) and 8(b). Additionally, they measured the thermoelectric properties and were able to calculate the figure of merit zT as a function of temperature for each sample. This is a classic example of the phase-boundary mapping approach applied to a ternary system. By making small compositional changes, the charge carrier concentration n can be tuned, leading to appreciable changes in the thermoelectric figure of merit zT. For instance, they showed that, by going from the composition $Ca_9Zn_{4.2}Sb_9$ to $Ca_9Zn_{4.6}Sb_9$, the zT triples from about 0.3 at 800 K to about 0.9 at 800 K, as a result of differing phase equilibria.

A. Using ternary phase-boundary mapping to understand dopability

A key consideration in designing better thermoelectric materials that was mentioned briefly in the discussion of PbTe is the dopability of a material. The dopability is defined as the maximum charge carrier concentration that can be achieved by adding a particular dopant material to the semiconductor system [14]. This dopability is related, but not identical to, the solubility limit. While the solubility limit is simply dependent on how much

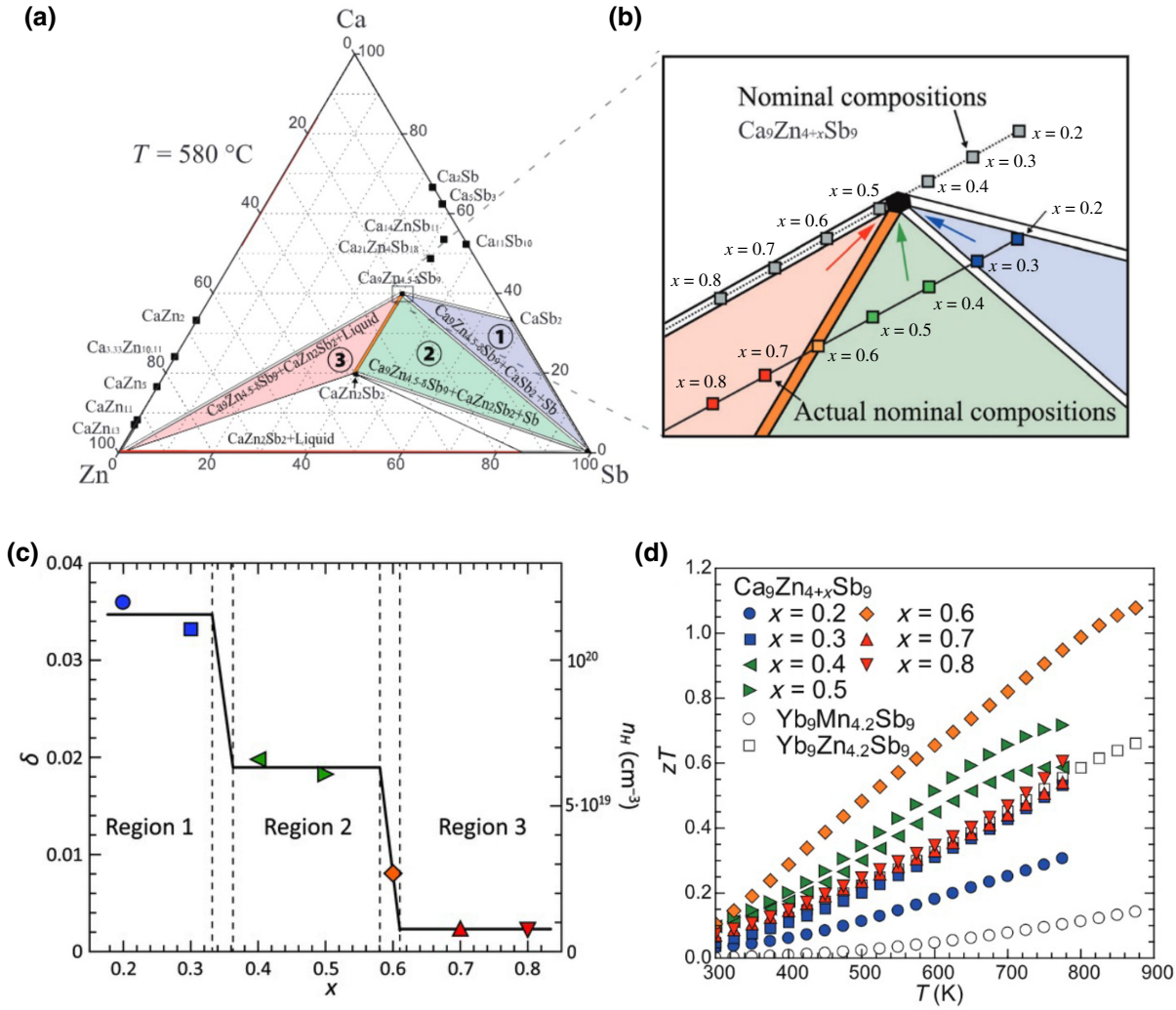

FIG. 8. Experimental phase-boundary mapping study conducted by Ohno *et al.* [15] on the Zintl phase $Ca_9Zn_{4+x}Sb_9$. (a) Phase diagram of the Ca-Zn-Sb ternary system with the three main phase regions of interest colored blue, green, and pink, respectively. (b) Enlarged region of the phase diagram in (a) that shows points for the different samples made in this study ($Ca_9Zn_{4+x}Sb_9$, with $x = 0.2$, 0.3, 0.4, 0.4, 0.6. 0.7, and 0.8). (c) Plot of the carrier concentration n_H versus composition. Here we can see that samples made in different phase regions have different charge carrier concentrations with a steplike function across phase boundaries. (d) Plot of zT versus temperature for each of the synthesized samples shown in the top phase diagrams. Small changes in composition can drastically change zT. Reprinted and adapted with permission from S. Ohno *et al.*, Adv. Funct. Mater. 27, 1606361 (2017). Copyright 2017, John Wiley and Sons.

dopant can be absorbed into the material, the dopability is impacted by both the solubility and also the resulting compensating defects. A compensating defect is the system's self-regulating attempt at charge neutrality. Since dopants introduce charge carriers, the system will tend to react by generating intrinsic compensating defects of the opposite charge. Thus, dopability is a direct result of defect energies. In order for a semiconducting material to be effectively doped, the defect formation energy of the dopant must be lower than the defect formation energies of the intrinsic defects in the material [91]. As discussed previously, the intrinsic defect formation energies depend on the chemical potential, which depends on phase equilibria. Thus, the dopability may be different in different phase regions, demonstrating once again the importance of understanding the phase region a sample is synthesized in.

It is important to remember however that the contributions of the defect formation energies are not always straightforward. Various complications introduced by intrinsic defects, secondary phase formation with the dopant atom, and Fermi-level pinning can constrain dopability. For instance, in the case of secondary phase formation, if the dopant forms a stable phase with the elements in

the host compound, there may be secondary phase formation that occurs upon doping to high levels that constrains the dopability past that point [92,93]. Fermi-level pinning can occur when compensating intrinsic defects form in response to doping, thus limiting the effect of doping and pinning the Fermi level at the point where these compensating "killer defects" completely negate the additional charge carriers coming from the dopant [92]. This was true in the case of Mg_3Sb_2 where low-energy Mg vacancies in Sb-excess samples made the material persistently *p* type despite efforts to dope *n* type. However, it was shown in the case of Mg_3Sb_2 that shifting the phase equilibria to Mg excess allowed for suppression of these Fermi-level pinning effects that once again demonstrates the importance of phase equilibria in doping thermoelectric materials [51]. However, Fermi-level pinning and other limiting effects on dopability are not always avoidable. In many traditional semiconductor systems, such as GaAs, dopability is constrained by these intrinsic defect effects [94].

While PbTe is a binary compound, when dopants are added it can be studied using ternary phase-boundary mapping approaches. In the case of the Pb-Te-I ternary system, we show in Fig. 9 that the dopability of I in PbTe is much greater when the sample is made Pb excess as opposed to Te excess. Conversely, in the case of the Pb-Te-Na ternary system, Te-excess samples are best for Na doping to obtain high *zT* *p*-type PbTe [53].

Another doping phase-boundary mapping study conducted using this ternary phase diagram approach was the study of Sn-doped ZnSb [16]. In this work, Wood *et al.* studied four distinct phase spaces about ZnSb in the Zn-Sb-Sn ternary phase diagram. They found that if samples were synthesized in chemical equilibrium with Zn_4Sb_3 and Sn, they obtained much higher carrier concentrations than if the Sn-doped ZnSb was synthesized in any of the other three-phase regions. Although the nominal compositions of the four synthesized samples differed by no more than 3 at. % for any of the three constituent atoms, these small changes in composition led to a fourfold increase in carrier concentration, optimizing the sample to the expected maximum *zT* determined by an effective mass model.

Their highest *zT* sample had distinguishable second phase regions in the microstructure of the expected phase equilibria phases of Zn_4Sb_3 and elemental Sn. Often in the field of thermoelectrics, much work is conducted to ensure that synthesized samples are as pure as possible with no distinguishable second phases. However, the danger with this approach, as elucidated by the phase-boundary mapping mindset, is that, for any given thermoelectric compound, there are at least two distinct thermodynamic states. By seeking out the most pure samples possible, it can be hard to determine the phase region synthesized. Thus, a thorough investigation of a thermoelectric material should include materials synthesized in the known phase regions to probe all possible thermodynamic states. In this case they were able to nearly double the *zT* by purposefully introducing those secondary phases to the material. Thus, the presence of secondary phases in a thermoelectric material is not always bad. Purposefully introducing secondary phases into the material can fix the chemical potential to a phase area that has more desirable defect energies for optimizing the charge carrier concentration or other related properties in the material.

B. Further ternary and multinary phase-boundary mapping studies

Not only can phase-boundary mapping be used to improve dopability of a material, but it can also be used in

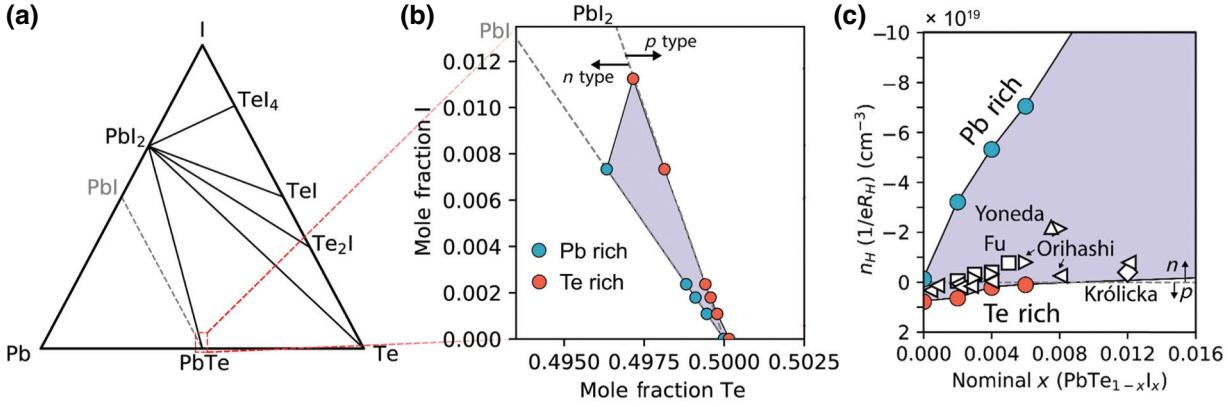

FIG. 9. Phase-boundary mapping study of I-doped PbTe. (a) Ternary phase diagram of the Pb-Te-I system. (b) Enlarged portion of the phase diagram about the compound PbTe. The blue points are samples that are Pb rich, leading to *n*-type behavior, while the red points are Te rich, leading to *p*-type behavior. (c) Plot of the carrier concentration (a negative sign signifies electrons as the charge carrier, and a positive sign signifies holes) with increasing iodine doping in PbTe. Here we see that samples that are Pb rich are very dopable *n* type with the addition of I, whereas the addition of I to Te-rich samples will not make a good *n*-type material. Reproduced with permission from J. Male *et al.*, Mater. Horiz. 6, 1444 (2019). Copyright 2019, Royal Society of Chemistry.

solubility design [12]. $CoSb_3$ (sometimes written Co_4Sb_{12}) is a skutterudite material that has void filling sites that can be filled with dopant alkaline-earth or rare-earth atoms such as Yb [95,96]. For these compounds, there exists a maximum ratio of dopants that can fill the structure that is called the filling fraction limit [12]. This filling fraction can be considered to be a solubility of Yb in $CoSb_3$. Using a phase-boundary mapping approach (although it was not called such), Tang *et al.* [12] showed that, as they synthesized $Yb_xCo_{4+y}Sb_{12+z}$ samples of differing compositions, the solubility of Yb changed depending on the region of the phase diagram in which the sample was synthesized; see Fig. 10. Similar studies of filling Co-Sb skutterudites with Ce and In have also been conducted using similar phase diagram approaches [54,59].

Phase-boundary mapping is also a useful tool to resolve large discrepancies in literature data regarding the thermoelectric properties. Since this phase equilibria approach is often not considered in thermoelectric synthesis, different studies may unintentionally be in different phase equilibria for the same nominal compound. Take the half-Heusler material TiNiSn for example. Prior to a 2018 phase-boundary mapping study [58], there were significant discrepancies in the literature regarding the solubility of Ni in TiNiSn. While it had been shown that excess Ni in TiNiSn leads to higher performance [55,97], the literature discrepancies regarding the solubility of Ti in TiNiSn were significant. By phase-boundary mapping, Tang *et al.* [58] were able to show that, by setting the chemical potential to the Ni-rich side of the phase space, they achieved a larger

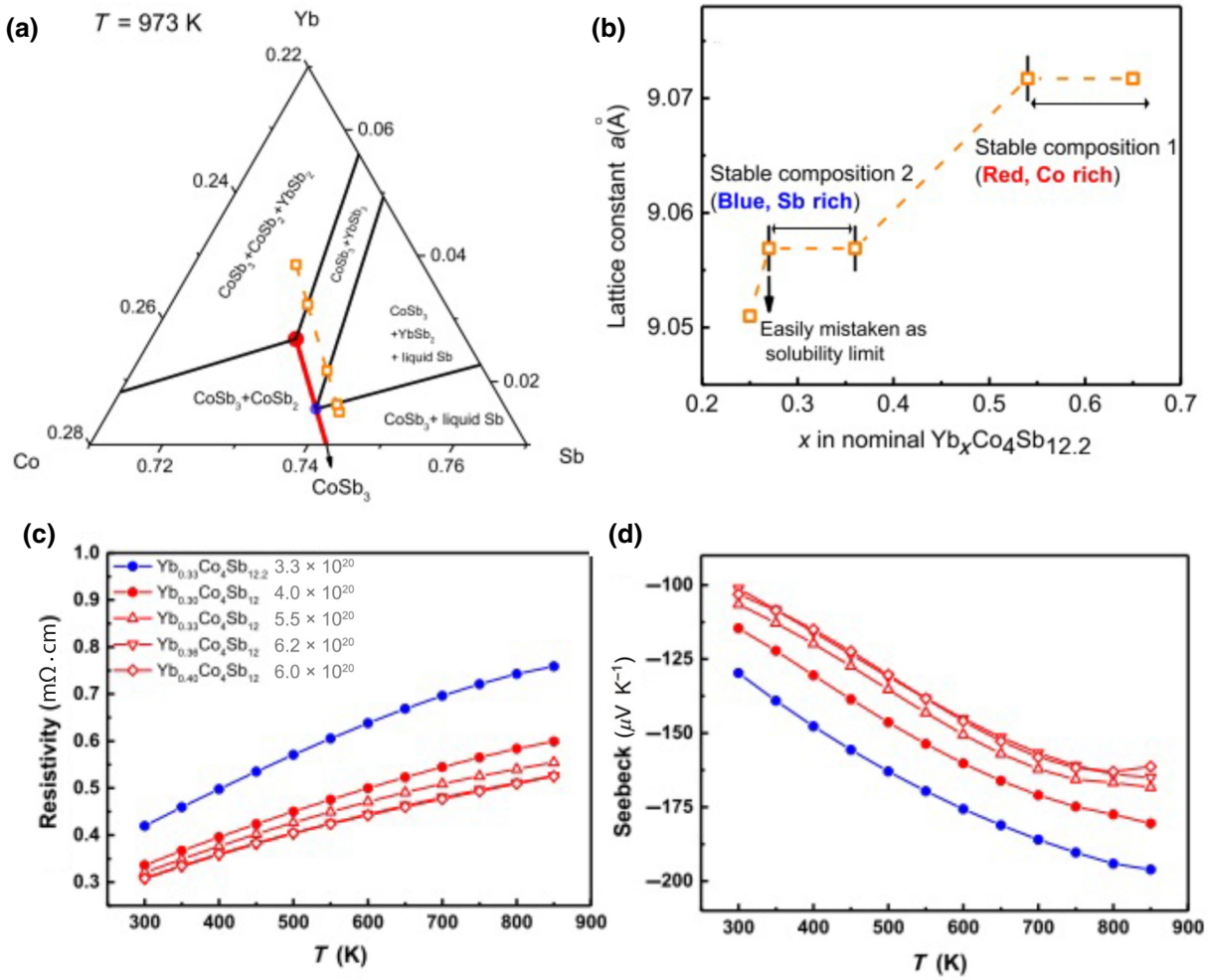

FIG. 10. Phase-boundary mapping study of $CoSb_3$. (a) Ternary phase diagram of the Yb-Co-Sb system. The orange points are experimental sample compositions. (b) Lattice constant as a function of the composition of $Yb_xCo_4Sb_{12.2}$. Here we see a step function as the composition crosses from being Sb excess to Co excess. (c) Resistivity as a function of temperature for differing compositions, with the Hall carrier density at 300 K for each sample in the top right corner. The Co-excess samples (red) have lower resistivities and higher charge carrier concentrations than the Sb-excess sample (blue). (d) Plot of the Seebeck coefficient versus temperature for the various sample compositions. The Sb-rich sample (blue) has a lower Seebeck coefficient than the Co-rich samples (red). Reprinted with permission from Y. Tang et al., J. Materiomics 1, 75 (2015). Copyright 2015, Elsevier.

zT, and they demonstrated the narrow solubility range of Ni in TiNiSn in the context of these small phase regions.

Another system with substantial discrepancies in the literature was the Mg_2Si-Mg_2Sn pseudobinary [98]. Phase-boundary mapping sets the chemical potentials in equilibrium. However, in a phase-boundary mapping study by Orenstein *et al.* [17] it was shown that many of the discrepancies in the literature were due to samples being out of equilibrium due to a loss of Mg in synthesis. The miscibility gap of the system changes depending on whether the system is Mg rich or not. This study demonstrated another success of phase-boundary mapping in reconciling differences between data from different studies for the same nominal compound.

Phase-boundary mapping is not limited to the consideration of binary and ternary phase diagrams. In a 2019 study by Ortiz *et al.* [19], they demonstrated the use of phase-boundary mapping on the quaternary Cu-Hg-Ge-Te phase diagram. This was the first study that considered a quaternary phase diagram using phase-boundary mapping, and it demonstrated the success of this method in identifying phase-region-dependent behavior of the charge carrier concentration, even for an exceptionally complicated material system. They found that the hole concentration in these thermoelectric materials ranged from 5×10^{17} to 5×10^{21} cm^{-3} depending on the phase equilibria. Thus, phase-boundary mapping has so far been demonstrated on binary, ternary, and quaternary systems, demonstrating its ability to apply to many, if not the majority of, thermoelectric material systems.

VII. PRACTICAL STEPS FOR FUTURE PHASE-BOUNDARY MAPPING STUDIES

In this tutorial we have given both the underlying physics and chemistry-based understanding of phase-boundary mapping as well as discussed many different studies that used this approach in the optimization of thermoelectric materials. Now we provide a practical guide to conducting future phase-boundary mapping studies. The key steps in any phase-boundary mapping study are consideration of the phase diagram, experimental material synthesis to set the chemical potentials and identify secondary phases, and interpretation and analysis of the results.

A. Determination of guiding phase diagram

The first step in any phase-boundary mapping study is to consider the phase diagrams and stable phases in the material system of interest. Databases like the Materials Project [99] and Open Quantum Materials Database [100,101] contain DFT-calculated phase diagrams for numerous binary, ternary, and even some multinary phase systems. It is important to note that such phase diagrams are calculated for the 0 K case, and may not be accurate at higher temperatures. Experimental phase diagrams may also be available via databases like the ASM Alloy Phase Diagram Database [102,103]. Here, the goal is to identify all possible secondary phases that may equilibrate with the target compound. In the case of a simple binary system with only one stable compound of interest as shown in the schematic in Fig. 3, the only phases on the phase diagram are the binary phase and the two constituent element phases. In most systems however it is more complicated.

It is also important in the consideration of these thermoelectric phase diagrams to do a thorough literature search of other possible phases that may not appear in these databases but have been experimentally reported. For instance, the Yb-Mn-Sb phase diagram is of importance to the thermoelectric community due to the high performing $Yb_{14}MnSb_{11}$ compound [104]. The Yb-Mn-Sb phase diagram is relatively complex, with multiple stable ternary and binary compounds, many of which are reported within DFT databases. However, some experimentally reported compounds such as $Yb_{10}MnSb_9$ [105,106] and $Yb_{21}Mn_4Sb_{18}$ [107] do not appear in these DFT-calculated phase diagrams. For this reason, it is important to consider all possible phases that could be present in the system, not just those found using a quick DFT database search. Once all of the phases of interest have been identified, the next step is to compile them into a single phase diagram using their reported stoichiometries. From there, the phase regions of interest about the compound of interest should be identified. In the study of a binary compound these regions may be as simple as "*A* excess" and "*B* excess," as shown in the schematic phase diagram in Fig. 3. In a ternary phase diagram there may be many phase regions to consider. Any phase region that is in equilibrium with the target phase should be considered for a thorough phase-boundary mapping study. For instance, in the sample ternary phase diagram shown in Fig. 5, even though there are nine total three-phase regions, only seven should be considered in phase-boundary mapping of the target phase labeled $A_xB_yC_z$. Once the possible phase regions have been identified, samples can be synthesized in various compositions and/or chemical potential states. However, it may not always be necessary to consider every single possible phase region. It has been shown that, given knowledge about an expected dominant defect in a material, the phase regions likely to have maximum and minimum defect concentrations can be predicted [108]. Yet, in cases where the dominant defect may not be known, or when multiple defects have similar energy, then a full phase-boundary mapping study considering all regions may be necessary.

B. Experimental synthesis and phase identification

There are a few different ways in which experimental samples for phase-boundary mapping can be synthesized.

Polycrystalline thermoelectric samples tend to be synthesized by combining stoichiometric ratios of elemental powders, pellets, or shavings and then reacting them via high-energy ball milling [109], melting in quartz tubes, and/or arc melting [110–112] followed by densification via hot pressing [113] or spark plasma sintering [114]. Perhaps the simplest method for phase-boundary mapping is to simply alter the stoichiometry of the sample when powders, pellets, or shavings of different elements are being measured out for synthesis. If these elemental powders fully react, the result will ideally be a matrix phase of the compound of interest with secondary phases as suggested by the phase diagram.

The identification of secondary phases is the best way to confirm which phase region a sample is in. Because some elements may be more or less likely to be "lost" during synthesis, simply relying on the measured nominal composition of the elements is not sufficient. For instance, in the phase-boundary mapping study of the $Ca_9Zn_{4+x}Sb_9$ compound, it was found that the actual compositions of samples varied from the measured nominal compositions used for synthesis due to a systematic loss of Ca during processing [15]. This systematic loss of an element during processing is not particularly uncommon. For instance, in the synthesis of Mg_3Sb_2, it has been shown that Mg loss always exists, perhaps due to oxidation during preparation or vaporization during hot pressing [51]. In order to identify these phases, it may be important to synthesize compositions far enough in compositional space from the boundary such that secondary phases are within the detection limits of phase identification experimental techniques.

Phase identification can be done using a variety of methods, most commonly x-ray diffraction (XRD), scanning electron microscopy (SEM), and energy dispersive spectroscopy (EDS) or energy probe microanalysis. Other homogeneity techniques such as scanning Seebeck measurements [79] may also be used. Each of these methods have their strengths and drawbacks. For instance, XRD is an incredibly common technique that is relatively easy to use. It is capable of identifying secondary phases through identifying extra peaks in the diffraction pattern. However, this becomes much more tricky if the secondary phases and the primary phase have complicated crystal structures with peaks with similar 2θ values. Additionally, many XRD setups have an impurity detection limit of the order of 5–10% [115], which may make this technique not as useful in many phase-boundary mapping studies. Additionally, the contrast in backscattering electron (BSE) SEM images can be used in conjunction with EDS to identify secondary phases. However, this BSE contrast is a result of compositional differences between phases. If the primary phase and the secondary phases are very close in compositional space, there may not be sufficient contrast between phases. However, in cases where the chemical compositions of secondary phases are sufficiently different, SEM is a good tool with good sensitivity to detect these secondary phases. Thus, in phase identification it may be necessary to use multiple techniques in conjunction with each other to fully characterize the sample. Similarly, some knowledge about the secondary phase crystal structures and composition will be necessary to select the best phase identification techniques for a particular material system.

Another experimental method of phase-boundary mapping is through saturation annealing, shown schematically in Fig. 11. This method is beneficial when compared to other phase-boundary mapping synthesis techniques in that it sets the chemical potential of the material without adding excessive secondary phases that may impact properties (often negatively). Furthermore, the addition of an excess specific element(s) may move the local composition out of the target equilibrium, leading to confusing results. This was discussed in the phase-boundary mapping study of the Mg_2Si-Mg_2Sn psuedobinary, where it was shown that the common strategy of adding excess Mg shifted local equilibrium, making phases with different compositions [17]. In this technique, a sample with the stoichiometry of the target compound is sealed in a tube with a saturating media that is excess in whichever component is chosen to be in equilibrium with the sample, in such a way that they are not physically touching each other (such as by having quartz wool between the stoichiometry sample and the saturating media) [14]. By annealing this sample, equilibrium can be reached between the stoichiometric

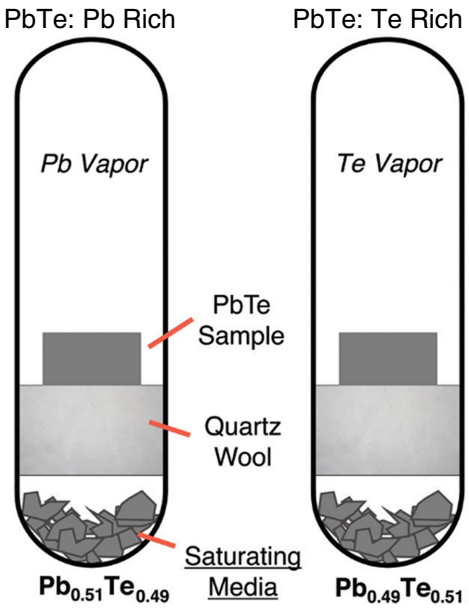

FIG. 11. Experimental setup for saturation annealing for phase-boundary mapping PbTe [14]. Reproduced with permission from J. Male *et al.*, Mater. Horiz. 6, 1444 (2019). Copyright 2019, Royal Society of Chemistry.

sample and the saturating media such that the chemical potential of the sample is fixed to that of the desired phase region. This saturation annealing can also be conducted with slightly different setups, such as saturation annealing in a MgO crucible in a graphite susceptor with induction heating [116].

A similar methodology was used for a phase-boundary-mapping-type study of GaAs, although it was not described as such. Hazama *et al.* [56] showed that they could change the chemical potentials of their GaAs samples by annealing them with an overpressure of As such that they obtained an As-excess sample. Similarly, it has been shown that, by controlling the partial pressure of Mg during annealing, Mg-vacancy concentrations could be changed as a means of tuning $Mg_{2-\delta}Si_{1-x}Sb_x$ [117].

While phase-boundary mapping can be done experimentally through a variety of different avenues, the important takeaway is that the chemical potential of the sample is set to a particular region of the phase diagram as different regions have different chemical potentials and defect energies.

C. Property determination and analysis

Once the thermoelectric samples have been synthesized such that each sample is set to a specific region in the phase diagram, standard thermoelectric property analysis is conducted. Generally, this involves measuring properties like the electrical conductivity σ, thermal conductivity κ, and the Seebeck coefficient α, in order to calculate zT. Additionally, measurements of the charge carrier concentration n via Hall effect measurements are often conducted. These transport measurements can be conducted using a variety of different specific setups [118], some of which are available via commercial instruments, and other setups requiring home-built instruments [119,120]. If one wants to extend this phase-boundary mapping approach to other types of defect-controlled materials such as photovoltaics or solid electrolytes [121], other transport and property measurements should be conducted.

Here, the experimentalist is checking for phase-region-dependent transport properties. For instance, in the case of Mg_3Sb_2, it was found that if the samples were made Mg excess, they exhibited n-type transport, whereas if the samples were made Sb excess, they exhibited p-type transport [51]. Step functions in thermoelectric properties across phase boundaries may be observed, as shown in Fig. 7. Additionally, this analysis can be aided by DFT calculations on defect formation energies [17,122]. Computationally determining the dominant defect in various phase regions can help explain the differences in the transport properties that are observed.

VIII. CONCLUSION

All thermoelectric compounds have at least two possible thermodynamic states, as indicated by the phase diagram. These states can have vastly different defect formation energies that may lead to different charge carrier concentrations, impact other defect-dependent properties, and sometimes even change the dominant charge carrier type. Since the thermoelectric figure of merit zT is very dependent on defect-related properties, such as the charge carrier concentration, the thermodynamic state of a material can have a profound impact on performance.

We have shown that phase-boundary mapping is an experimental methodology in which these distinct thermodynamic states of the same compound are systematically explored. By synthesizing materials in different phase equilibria, the full potential of the thermoelectric material can be studied. Too often, researchers studying thermoelectrics fail to recognize the importance of phase equilibria, often limiting the performance of their materials, or resulting in conflicting or unreproducible results. Phase-boundary mapping can be used on nearly any thermoelectric material system and is a necessary step in thermoelectric studies and optimization. While we have discussed many recent studies of phase-boundary mapping thermoelectric materials in this tutorial, there are still many promising thermoelectric materials that have not yet been studied using phase-boundary mapping that could benefit greatly from this approach.

Additionally, phase-boundary mapping is not just relevant for thermoelectric materials. Studies of other complex semiconductor materials such as those for photovoltaics could benefit from this approach. In short, any type of functional material where the properties are dominated by defects could make use of these approaches. For instance, in most electronic materials and photovoltaics, there is a strong dependence on carrier concentration to achieve optimal behavior. This is often tuned through doping. However, this phase-boundary mapping approach shows us that, due to differing chemical potentials, carrier concentrations and dopability can vary depending on the phase region of synthesis. Optimally doping other types of functional materials could benefit from this phase-boundary mapping approach.

ACKNOWLEDGMENTS

L.B. is supported by the National Science Foundation Graduate Research Fellowship Program under Grant No. DGE-1842165. Any opinions, findings, and conclusions or recommendations expressed in this material are those of the author(s) and do not necessarily reflect the views of the National Science Foundation. We also acknowledge financial assistance from the U.S. Department of Commerce under Grant No. 70NANB19H005, the National Institute of Standards and Technology as part of the Center for Hierarchical Materials Design (CHiMaD), as well as the NSF DMREF under Grant No. 1729487.

L.B. first drafted the manuscript. All authors contributed to the preparation and editing of the manuscript. G.J.S. supervised the work and proposed the scope.

[1] G. J. Snyder and E. S. Toberer, Complex thermoelectric materials, Nat. Mater. **7**, 105 (2008).

[2] T. C. Holgate, R. Bennett, T. Hammel, T. Caillat, S. Keyser, and B. Sievers, Increasing the efficiency of the multi-mission radioisotope thermoelectric generator, J. Electron. Mater. **44**, 1814 (2015).

[3] S. LeBlanc, Thermoelectric generators: Linking material properties and systems engineering for waste heat recovery applications, Sustainable Mater. Technol. **1**, 26 (2014).

[4] L. E. Bell, Cooling, heating, generating power, and recovering waste heat with thermoelectric systems, Science **321**, 1457 (2008).

[5] L. S. Hewawasam, A. S. Jayasena, M. M. M. Afnan, R. A. C. P. Ranasinghe, and M. A. Wijewardane, Waste heat recovery from thermo-electric generators (TEGs), Energy Rep. **6**, 474 (2019).

[6] F. J. Disalvo, Thermoelectric cooling and power generation, Science **285**, 703 (1999).

[7] G. J. Snyder, S. LeBlanc, D. Crane, H. Pangborn, C. E. Forest, A. Rattner, L. Borgsmiller, and S. Priya, Distributed and localized cooling with thermoelectrics, Joule **5**, 748 (2021).

[8] D. Rowe, ed.,*CRC Handbook of Thermoelectrics* (CRC/Taylor & Francis, Boca Raton, 1995).

[9] G. Libowitz, Nonstoichiometry in chemical compounds, Prog. Solid State Chem. **2**, 216 (1965).

[10] S. Ohno, Ph.D. thesis, California Institute of Technology, 2017.

[11] I. T. Witting, T. C. Chasapis, F. Ricci, M. Peters, N. A. Heinz, G. Hautier, and G. J. Snyder, The thermoelectric properties of bismuth telluride, Adv. Electron. Mater. **5**, 1800904 (2019).

[12] Y. Tang, S. wen Chen, and G. J. Snyder, Temperature dependent solubility of Yb in Yb–$CoSb_3$ skutterudite and its effect on preparation, optimization and lifetime of thermoelectrics, J. Materiomics **1**, 75 (2015).

[13] S. Anand, J. P. Male, C. Wolverton, and G. J. Snyder, Visualizing defect energetics, Mater. Horiz. **8**, 1966 (2021).

[14] J. Male, M. T. Agne, A. Goyal, S. Anand, I. T. Witting, V. Stevanović, and G. J. Snyder, The importance of phase equilibrium for doping efficiency: Iodine doped PbTe, Mater. Horiz. **6**, 1444 (2019).

[15] S. Ohno, U. Aydemir, M. Amsler, J. H. Pöhls, S. Chanakian, A. Zevalkink, M. A. White, S. K. Bux, C. Wolverton, and G. J. Snyder, Achieving $zT > 1$ in inexpensive zintl phase $Ca_9Zn_{4+x}Sb_9$ by phase boundary mapping, Adv. Funct. Mater. **27**, 1606361 (2017).

[16] M. Wood, M. Y. Toriyama, S. Dugar, J. Male, S. Anand, V. Stevanović, and G. J. Snyder, Phase boundary mapping of tin-doped ZnSb reveals thermodynamic route to high thermoelectric efficiency, Adv. Energy Mater. **11**, 2100181 (2021).

[17] R. Orenstein, J. P. Male, M. Toriyama, S. Anand, and G. J. Snyder, Using phase boundary mapping to resolve discrepancies in the Mg_2Si–Mg_2Sn miscibility gap, J. Mater. Chem. **A**, 7208 (2021).

[18] X. Li, P. Yang, Y. Wang, Z. Zhang, D. Qin, W. Xue, C. Chen, Y. Huang, X. Xie, X. Wang, M. Yang, C. Wang, F. Cao, J. Sui, X. Liu, and Q. Zhang, Phase boundary mapping in ZrNiSn half-Heusler for enhanced thermoelectric performance, Research **2020**, 1 (2020).

[19] B. R. Ortiz, K. Gordiz, L. C. Gomes, T. Braden, J. M. Adamczyk, J. Qu, E. Ertekin, and E. S. Toberer, Carrier density control in $Cu_2HgGeTe_4$ and discovery of Hg_2GeTe_4: Via phase boundary mapping, J. Mater. Chem. A **7**, 621 (2019).

[20] K. F. Hsu, S. Loo, F. Guo, W. Chen, J. S. Dyck, C. Uher, T. Hogan, E. K. Polychroniadis, and M. G. Kanatzidis, Cubic $AgPb_mSbTe_{2+m}$: Bulk thermoelectric materials with high figure of merit, Science **303**, 818 (2004).

[21] J. Wei, L. Yang, Z. Ma, P. Song, M. Zhang, J. Ma, F. Yang, and X. Wang, Review of current high-ZT thermoelectric materials, J. Mater. Sci. **55**, 12642 (2020).

[22] C. Zhou, Y. K. Lee, Y. Yu, S. Byun, Z.-Z. Luo, H. Lee, B. Ge, Y.-L. Lee, X. Chen, J. Y. Lee, O. Cojocaru-Mirédin, H. Chang, J. Im, S.-P. Cho, M. Wuttig, V. P. Dravid, M. G. Kanatzidis, and I. Chung, Polycrystalline SnSe with a thermoelectric figure of merit greater than the single crystal, Nat. Mater. **20**, 1378 (2021).

[23] A. Zevalkink, E. S. Toberer, W. G. Zeier, E. Flage-Larsen, and G. J. Snyder, Ca_3AlSb_3: An inexpensive, non-toxic thermoelectric material for waste heat recovery, Energy Environ. Sci. **4**, 510 (2011).

[24] M. Cutler, J. F. Leavy, and R. L. Fitzpatrick, Electronic transport in semimetallic cerium sulfide, Phys. Rev. **133**, A1143 (1964).

[25] B. C. Sales, Electron crystals and phonon glasses: A new path to improved thermoelectric materials, MRS Bull. **23**, 15 (1998).

[26] R. Gurunathan, R. Hanus, and G. J. Snyder, Alloy scattering of phonons, Mater. Horiz. **7**, 1452 (2020).

[27] Y. I. Ravich, B. A. Efimova, and I. A. Smirnov, *Semiconducting Lead Chalcogenides* (Springer USA, New York, 1970), 1st ed.

[28] M. S. Dresselhaus, G. Chen, M. Y. Tang, R. Yang, H. Lee, D. Wang, Z. Ren, J. P. Fleurial, and P. Gogna, New directions for low-dimensional thermoelectric materials, Adv. Mater. **19**, 1043 (2007).

[29] B. Poudel, Q. Hao, Y. Ma, Y. Lan, A. Minnich, B. Yu, X. Yan, D. Wang, A. Muto, D. Vashaee, X. Chen, J. Liu, M. S. Dresselhaus, G. Chen, and Z. Ren, High-thermoelectric performance of nanostructured bismuth antimony telluride bulk alloys, Science **320**, 634 (2008).

[30] X. Li and R. Yang, Equilibrium molecular dynamics simulations for the thermal conductivity of Si/Ge nanocomposites, J. Appl. Phys. **113**, 21 (2013).

[31] E. S. Toberer, A. F. May, and G. J. Snyder, Zintl chemistry for designing high efficiency thermoelectric materials, Chem. Mater. **22**, 624 (2010).

[32] X. Zhang, Z. Bu, X. Shi, Z. Chen, S. Lin, B. Shan, M. Wood, A. H. Snyder, L. Chen, G. J. Snyder, and Y. Pei, Electronic quality factor for thermoelectrics, Sci. Adv. **6**, 6 (2020).

[33] Y. Pei, H. Wang, and G. J. Snyder, Band engineering of thermoelectric materials, Adv. Mater. **24**, 6125 (2012).

[34] S. D. Kang and G. J. Snyder, Transport property analysis method for thermoelectric materials: Material quality factor and the effective mass model (2017).

[35] G. J. Snyder, A. H. Snyder, M. Wood, R. Gurunathan, B. H. Snyder, and C. Niu, Weighted mobility, Adv. Mater. **32**, 1 (2020).

[36] F. A. Kröger and H. J. Vink, (Academic Press, Cambridge, MA, USA, 1956), p. 307.

[37] H. S. Kim, N. A. Heinz, Z. M. Gibbs, Y. Tang, S. D. Kang, and G. J. Snyder, High thermoelectric performance in $(Bi_{0.25}Sb_{0.75})_2Te_3$ due to band convergence and improved by carrier concentration control, Mater. Today **20**, 452 (2017).

[38] H. Wang, X. Cao, Y. Takagiwa, and G. J. Snyder, Higher mobility in bulk semiconductors by separating the dopants from the charge-conducting band - A case study of thermoelectric PbSe, Mater. Horiz. **2**, 323 (2015).

[39] M. Lannoo, *Point Defects in Semiconductors I: Theoretical Aspects*, Springer Series in Solid-State Sciences, 22 (Springer Berlin Heidelberg, Berlin, Heidelberg, 1981), 1st ed.

[40] W. Cai and W. D. Nix, *Imperfections in Crystalline Solids* (Cambridge University Press, Cambridge, UK, 2016).

[41] J. W. Fergus, Electrolytes for solid oxide fuel cells, J. Power Sources **162**, 30 (2006).

[42] J. Koettgen, S. Grieshammer, P. Hein, B. O. Grope, M. Nakayama, and M. Martin, Understanding the ionic conductivity maximum in doped ceria: Trapping and blocking, Phys. Chem. Chem. Phys. **20**, 14291 (2018).

[43] R. Bullough and R. C. Newman, The kinetics of migration of point defects to dislocations, Rep. Prog. Phys. **33**, 101 (1970).

[44] J. P. Male, L. Abdellaoui, Y. Yu, S. Zhang, N. Pieczulewski, O. Cojocaru-Mirédin, C. Scheu, and G. J. Snyder, Dislocations stabilized by point defects increase brittleness in PbTe, Adv. Funct. Mater. **2108006**, 1 (2021).

[45] H. L. Tuller and S. R. Bishop, Point defects in oxides: Tailoring materials through defect engineering, Annu. Rev. Mater. Res. **41**, 369 (2011).

[46] H. Xiao and I. Baker, The relationship between point defects and mechanical properties in Fe-Al at room temperature, Acta Metall. Mater. **43**, 391 (1995).

[47] R. Gurunathan, S. Anand, T. Soldi, L. Borgsmiller, R. Orenstein, and G. J. Snyder, Thermoelectric transport of semiconductor full-Heusler VFe_2Al, J. Mater. Chem. C **8**, 10174 (2020).

[48] A. Berche, M. T. Noutack, M. L. Doublet, and P. Jund, Unexpected band gap increase in the Fe_2VAl Heusler compound, Mater. Today Phys. **13**, 100203 (2020).

[49] G. Tan, S. Hao, R. C. Hanus, X. Zhang, S. Anand, T. P. Bailey, A. J. Rettie, X. Su, C. Uher, V. P. Dravid, G. J. Snyder, C. Wolverton, and M. G. Kanatzidis, High thermoelectric performance in $SnTe\text{-}AgSbTe_2$ alloys from lattice softening, giant phonon-vacancy scattering, and valence band convergence, ACS Energy Lett. **3**, 705 (2018).

[50] L. Fu, M. Yin, D. Wu, W. Li, D. Feng, L. Huang, and J. He, Large enhancement of thermoelectric properties in n-type PbTe *via* dual-site point defects, Energy Environ. Sci. **10**, 2030 (2017).

[51] S. Ohno, K. Imasato, S. Anand, H. Tamaki, S. D. Kang, P. Gorai, H. K. Sato, E. S. Toberer, T. Kanno, and G. J. Snyder, Phase boundary mapping to obtain *n*-type Mg_3Sb_2-based thermoelectrics, Joule **2**, 141 (2018).

[52] C. M. Crawford, B. R. Ortiz, P. Gorai, V. Stevanovic, and E. S. Toberer, Experimental and computational phase boundary mapping of $Co_4Sn_6Te_6$, J. Mater. Chem. A **6**, 24175 (2018).

[53] P. Jood, J. P. Male, S. Anand, Y. Matsushita, Y. Takagiwa, M. G. Kanatzidis, G. J. Snyder, and M. Ohta, Na doping in PbTe: Solubility, band convergence, phase boundary mapping, and thermoelectric properties, J. Am. Chem. Soc. **142**, 15464 (2020).

[54] Y. Tang, Y. Qiu, L. Xi, X. Shi, W. Zhang, L. Chen, S. M. Tseng, S. W. Chen, and G. J. Snyder, Phase diagram of In-Co-Sb system and thermoelectric properties of In-containing skutterudites, Energy Environ. Sci. **7**, 812 (2014).

[55] H. Hazama, M. Matsubara, R. Asahi, and T. Takeuchi, Improvement of thermoelectric properties for half-Heusler TiNiSn by interstitial Ni defects, J. Appl. Phys. **110**, 1 (2011).

[56] S. B. Zhang and J. E. Northrup, Chemical Potential Dependence of Defect Formation Energies in GaAs: Application to Ga Self-Diffusion, Phys. Rev. Lett. **67**, 2339 (1991).

[57] S. Lany and A. Zunger, Dopability, Intrinsic Conductivity, and Nonstoichiometry of Transparent Conducting Oxides, Phys. Rev. Lett. **98**, 2 (2007).

[58] Y. Tang, X. Li, L. H. Martin, E. Cuervo Reyes, T. Ivas, C. Leinenbach, S. Anand, M. Peters, G. J. Snyder, and C. Battaglia, Impact of Ni content on the thermoelectric properties of half-Heusler TiNiSn, Energy Environ. Sci. **11**, 311 (2018).

[59] Y. Tang, R. Hanus, S. W. Chen, and G. J. Snyder, Solubility design leading to high figure of merit in low-cost Ce-$CoSb_3$ skutterudites, Nat. Commun. **6**, 1 (2015).

[60] J. Corish, in *Defects and Disorder in Crystalline and Amorphous Solids* (Kluwer Academic Publisher, Dordrecht, Netherlands, 1994), p. 413.

[61] H. G. Deming, An introduction to the phase rule. Part I, J. Chem. Educ. **16**, 215 (1939).

[62] R. DeHoff, *Thermodynamics in Materials Science* (CRC Press, Boca Raton, FL, USA, 2006).

[63] G. S. Pomrehn, A. Zevalkink, W. G. Zeier, A. Van De Walle, and G. J. Snyder, Defect-controlled electronic properties in AZn_2Sb_2 Zintl phases, Angew. Chem. **53**, 3422 (2014).

[64] C. G. Van De Walle, D. B. Laks, G. F. Neumark, and S. T. Pantelides, First-principles calculations of solubilities and doping limits: Li, Na, and N in ZnSe, Phys. Rev. B **47**, 9425 (1993).

[65] C. Freysoldt, B. Grabowski, T. Hickel, J. Neugebauer, G. Kresse, A. Janotti, and C. G. Van De Walle, First-principles calculations for point defects in solids, RMP **86**, 253 (2014).

[66] R. Gurunathan, R. Hanus, M. Dylla, A. Katre, and G. J. Snyder, Analytical Models of Phonon-Point-Defect Scattering, Phys. Rev. Appl. **13**, 1 (2020).

[67] Y. Pei, L. Zheng, W. Li, S. Lin, Z. Chen, Y. Wang, X. Xu, H. Yu, Y. Chen, and B. Ge, Interstitial point defect scattering contributing to high thermoelectric performance in SnTe, Adv. Electron. Mater. **2**, 1 (2016).

[68] A. D. Lalonde, Y. Pei, H. Wang, and G. Jeffrey Snyder, Lead telluride alloy thermoelectrics, Mater. Today **14**, 526 (2011).

[69] D. Beretta, N. Neophytou, J. M. Hodges, M. G. Kanatzidis, D. Narducci, M. Martin-Gonzalez, M. Beekman, B. Balke, G. Cerretti, W. Tremel, A. Zevalkink, A. I. Hofmann, C. Müller, B. Dörling, M. Campoy-Quiles, and M. Caironi, Thermoelectrics: From history, a window to the future, Mater. Sci. Eng., R **138**, 210 (2019).

[70] R. D. Abelson, in *Thermoelectric Handbook: Macro to Nano*, edited by D. M. Rowe (CRC/Taylor & Francis, Boca Raton, 2006), p. 56–1–7.

[71] R. F. Brebrick and R. Allgaier, Composition stability limits of PbTe, J. Chem. Phys. **32**, 1826 (1960).

[72] R. F. Brebrick and E. Gubner, Composition stability limits of PbTe. II, J. Chem. Phys. **36**, 1283 (1962).

[73] C. R. Hewes, M. S. Adler, and S. D. Senturia, Annealing studies of PbTe and $Pb_{1-x}Sn_xTe$, J. Appl. Phys. **44**, 1327 (1972).

[74] B. J. Sealy and A. J. Crocker, The *P-T-x* phase diagram of PbTe and PbSe, J. Mater. Sci **8**, 1737 (1973).

[75] W. W. Scanlon, Precipitation of Te and Pb in PbTe crystals, Phys. Rev. **126**, 509 (1962).

[76] S. Bajaj, G. S. Pomrehn, J. W. Doak, W. Gierlotka, H. J. Wu, S. W. Chen, C. Wolverton, W. A. Goddard, and G. Jeffrey Snyder, Ab initio study of intrinsic point defects in PbTe: An insight into phase stability, Acta Mater. **92**, 72 (2015).

[77] A. Goyal, P. Gorai, E. S. Toberer, and V. Stevanović, First-principles calculation of intrinsic defect chemistry and self-doping in PbTe, Npj Comput. Mater. **3**, 1 (2017).

[78] M. C. Peters, J. W. Doak, W. W. Zhang, J. E. Saal, G. B. Olson, and P. W. Voorhees, Thermodynamic modeling of the PbX (X=S, Te) phase diagram using a five sub-lattice and two sub-lattice model, CALPHAD **58**, 17 (2017).

[79] S. Iwanaga and G. J. Snyder, Scanning Seebeck coefficient measurement system for homogeneity characterization of bulk and thin-film thermoelectric materials, J. Electron. Mater. **41**, 1667 (2012).

[80] G. R. Miller and C. Y. Li, Evidence for the existence of antistructure defects in bismuth telluride by density measurements, J. Phys. Chem. Solids **26**, 173 (1965).

[81] M. W. Oh, J. H. Son, B. S. Kim, S. D. Park, B. K. Min, and H. W. Lee, Antisite defects in *n*-type $Bi_2(Te,Se)_3$: Experimental and theoretical studies, J. Appl. Phys. **115**, 133706 (2014).

[82] D. O. Scanlon, P. D. King, R. P. Singh, A. De La Torre, S. M. K. Walker, G. Balakrishnan, F. Baumberger, and C. R. Catlow, Controlling bulk conductivity in topological insulators: Key role of anti-site defects, Adv. Mater. **24**, 2154 (2012).

[83] C. L. Condron, S. M. Kauzlarich, F. Gascoin, and G. J. Snyder, Thermoelectric properties and microstructure of Mg_3Sb_2, J. Solid State Chem. **179**, 2252 (2006).

[84] A. Bhardwaj, A. Rajput, A. K. Shukla, J. J. Pulikkotil, A. K. Srivastava, A. Dhar, G. Gupta, S. Auluck, D. K. Misra, and R. C. Budhani, Mg_2Sb_2-based Zintl compound: A non-toxic, inexpensive and abundant thermoelectric material for power generation, RSC Adv. **3**, 8504 (2013).

[85] A. Bhardwaj, N. S. Chauhan, S. Goel, V. Singh, J. J. Pulikkotil, T. D. Senguttuvan, and D. K. Misra, Tuning the carrier concentration using Zintl chemistry in Mg_3Sb_2, and its implications for thermoelectric figure-of-merit, Phys. Chem. Chem. Phys. **18**, 6191 (2016).

[86] S. A. Miller, M. Dylla, S. Anand, K. Gordiz, G. J. Snyder, and E. S. Toberer, Empirical modeling of dopability in diamond-like semiconductors, Npj Comput. Mater. **4**, 1 (2018).

[87] A. Zevalkink, W. G. Zeier, E. Cheng, J. Snyder, J. P. Fleurial, and S. Bux, Nonstoichiometry in the zintl phase $Yb_{1-\delta}Zn_2Sb_2$ as a route to thermoelectric optimization, Chem. Mater. **26**, 5710 (2014).

[88] R. F. Brebrick, Composition stability limits rocksalt-structure phase $(Pb_{1-y}Sn_y)_{1-x}Te_x$ from lattice parameter measurements, J. Phys. Chem. Solids **32**, 551 (1971).

[89] V. L. Kuznetsov, System Sn-Te: Critical evaluation and optimization of data on the thermodynamic properties and phase diagram, Inorg. Mater. **32**, 231 (1996).

[90] R. F. Brebrick, Deviations from stoichiometry and electrical properties in SnTe, J. Phys. Chem. Solids **24**, 27 (1963).

[91] P. Gorai, V. Stevanović, and E. S. Toberer, Computationally guided discovery of thermoelectric materials, Nat. Rev. Mater. **2**, 1 (2017).

[92] A. Walsh and A. Zunger, Instilling defect tolerance in new compounds, Nat. Mater. **16**, 964 (2017).

[93] D. Horwat, M. Jullien, F. Capon, J. F. Pierson, J. Andersson, and J. L. Endrino, On the deactivation of the dopant and electronic structure in reactively sputtered transparent Al-doped ZnO thin films, J. Phys. D: Appl. Phys. **43**, 132003 (2010).

[94] W. Walukiewicz, Intrinsic limitations to the doping of wide-gap semiconductors, Physica B **302-303**, 123 (2001).

[95] X. Y. Zhao, X. Shi, L. D. Chen, W. Q. Zhang, S. Q. Bai, Y. Z. Pei, X. Y. Li, and T. Goto, Synthesis of $Yb_yCo_4Sb_{12}/Yb_2O_3$ composites and their thermoelectric properties, Appl. Phys. Lett. **89**, 092121 (2006).

[96] H. Li, X. Tang, Q. Zhang, and C. Uher, Rapid preparation method of bulk nanostructured $Yb_{0.3}Co_4Sb_{12+y}$ compounds and their improved thermoelectric performance, Appl. Phys. Lett. **93**, 3 (2008).

[97] C. S. Birkel, J. E. Douglas, B. R. Lettiere, G. Seward, N. Verma, Y. Zhang, T. M. Pollock, R. Seshadri, and G. D. Stucky, Improving the thermoelectric properties of half-Heusler TiNiSn through inclusion of a second full-Heusler phase: Microwave preparation and spark plasma sintering of $TiNi_{1+x}Sn$, Phys. Chem. Chem. Phys. **15**, 6990 (2013).

[98] M. Yasseri, A. Sankhla, H. Kamila, R. Orenstein, D. Y. Truong, N. Farahi, J. de Boor, and E. Mueller, Solid solution formation in $Mg_2(Si,Sn)$ and shape of the miscibility gap, Acta Mater. **185**, 80 (2020).

[99] A. Jain, S. P. Ong, G. Hautier, W. Chen, W. D. Richards, S. Dacek, S. Cholia, D. Gunter, D. Skinner, G. Ceder, and K. a. Persson, The Materials Project: A materials genome

approach to accelerating materials innovation, APL Mater. **1**, 011002 (2013).

[100] J. E. Saal, S. Kirklin, M. Aykol, B. Meredig, and C. Wolverton, Materials design and discovery with high-throughput density functional theory: The open quantum materials database (OQMD), JOM **65**, 1501 (2013).

[101] S. Kirklin, J. E. Saal, B. Meredig, A. Thompson, J. W. Doak, M. Aykol, S. Rühl, and C. Wolverton, The Open Quantum Materials Database (OQMD): Assessing the accuracy of DFT formation energies, Npj Comput. Mater. **1**, 15010 (2015).

[102] P. Villars, A. Prince, and H. Okamoto, *Handbook of Ternary Alloy Phase Diagrams* (American society for metals, Materials Park, OH, USA, 1995).

[103] P. Villars, H. Okamoto, and K. Cenzual, ASM alloy phase diagrams center, ASM International, Materials Park (2006).

[104] S. R. Brown, S. M. Kauzlarich, F. Gascoin, and G. Jeffrey Snyder, $Yb_{14}MnSb_{11}$: New high efficiency thermoelectric material for power generation, Chem. Mater. **18**, 1873 (2006).

[105] S. Baranets, A. Ovchinnikov, and S. Bobev, Complex structural disorder in the Zintl phases $Yb_{10}MnSb_9$ and $Yb_{21}Mn_4Sb_{18}$, Inorg. Chem. **60**, 6702 (2021).

[106] L. Borgsmiller and G. J. Snyder, Thermoelectric properties and low thermal conductivity of Zintl compound $Yb_{10}MnSb_9$, J. Mater. Chem. A **10**, 15127 (2022).

[107] A. He, S. K. Bux, Y. Hu, D. Uhl, L. Li, D. Donadio, and S. M. Kauzlarich, Structural complexity and high thermoelectric performance of the Zintl phase: $Yb_{21}Mn_4Sb_{18}$, Chem. Mater. **31**, 8076 (2019).

[108] S. Anand, C. Wolverton, and G. J. Snyder, Thermodynamic guidelines for maximum solubility, Chem. Mater. **34**, 1638 (2022).

[109] J. H. Son, M. W. Oh, B. S. Kim, S. D. Park, B. K. Min, M. H. Kim, and H. W. Lee, Effect of ball milling time on the thermoelectric properties of p-type $(Bi, Sb)_2Te_3$, J. Alloys Compd. **566**, 168 (2013).

[110] J. Gainza, F. Serrano-Sánchez, J. E. Rodrigues, Y. Huttel, O. J. Dura, M. M. Koza, M. T. Fernández-Díaz, J. J. Meléndez, B. G. Márkus, F. Simon, J. L. Martínez, J. A. Alonso, and N. M. Nemes, High-performance n-type SnSe thermoelectric polycrystal prepared by arc-melting, Cell Rep. Phys. Sci. **1**, 100263 (2020).

[111] Y. Kawaharada, K. Kurosaki, M. Uno, and S. Yamanaka, Thermoelectric properties of $CoSb_3$, J. Alloys Compd. **315**, 193 (2001).

[112] H. Anno, H. Yamada, T. Nakabayashi, M. Hokazono, and R. Shirataki, Gallium composition dependence of crystallographic and thermoelectric properties in polycrystalline type-I $Ba_8Ga_xSi_{46-x}$ (nominal $x = 14$-18) clathrates prepared by combining arc melting and spark plasma sintering methods, J. Solid State Chem. **193**, 94 (2012).

[113] A. D. LaLonde, T. Ikeda, and G. J. Snyder, Rapid consolidation of powdered materials by induction hot pressing, Rev. Sci. Instrum. **82**, 1 (2011).

[114] Z. Munir, U. Anselmi-Tamburini, and M. Ohyanagi, The effect of electric field and pressure on the synthesis and consolidation of materials: A review of the spark plasma sintering method, J. Mater. Sci. **41**, 763 (2006).

[115] C. F. Holder and R. E. Schaak, Tutorial on powder x-ray diffraction for characterizing nanoscale materials, ACS Nano **13**, 7359 (2019).

[116] M. Wood, J. J. Kuo, K. Imasato, and G. J. Snyder, Improvement of low-temperature zT in a Mg_3Sb_2–Mg_3Bi_2 solid solution via Mg-vapor annealing, Adv. Mater. **31**, 1902337 (2019).

[117] D. Kato, K. Iwasaki, M. Yoshino, T. Yamada, and T. Nagasaki, Significant effect of Mg-pressure-controlled annealing: Non-stoichiometry and thermoelectric properties of $Mg_{2-\delta}Si_{1-x}Sb_x$, Phys. Chem. Chem. Phys. **20**, 25939 (2018).

[118] H. Wang, W. D. Porter, H. Böttner, J. König, L. Chen, S. Bai, T. M. Tritt, A. Mayolet, J. Senawiratne, C. Smith, F. Harris, P. Gilbert, J. W. Sharp, J. Lo, H. Kleinke, and L. Kiss, Transport properties of bulk thermoelectrics—An international round-robin study, part I: Seebeck coefficient and electrical resistivity, J. Electron. Mater. **42**, 654 (2013).

[119] K. A. Borup, E. S. Toberer, L. D. Zoltan, G. Nakatsukasa, M. Errico, J. P. Fleurial, B. B. Iversen, and G. J. Snyder, Measurement of the electrical resistivity and Hall coefficient at high temperatures, Rev. Sci. Instrum. **83**, 123902 (2012).

[120] S. Iwanaga, E. S. Toberer, A. Lalonde, and G. J. Snyder, A high temperature apparatus for measurement of the Seebeck coefficient, Rev. Sci. Instrum. **82**, 063905 (2011).

[121] M. Shimoda, M. Maegawa, S. Yoshida, H. Akamatsu, K. Hayashi, P. Gorai, and S. Ohno, Controlling defects to achieve reproducibly high ionic conductivity in Na_3SbS_4 solid electrolytes, Chem. Mater. **34**, 5634 (2022).

[122] M. Y. Toriyama, J. Qu, G. J. Snyder, and P. Gorai, Defect chemistry and doping of BiCuSeO, J. Mater. Chem. A **9**, 20685 (2021).